Journal of Photochemistry & Photobiology, A: Chemistry 432 (2022) 114106

Contents lists available at ScienceDirect

Journal of Photochemistry & Photobiology, A: Chemistry

journal homepage: www.elsevier.com/locate/jphotochem

Synthesis of $NiFe_2O_4/TiO_2$-Ag^+ S-scheme photocatalysts by a novel complex-assisted vapor thermal method for photocatalytic hydrogen production

Irem Firtina-Ertis [a,*], Özge Kerkez-Kuyumcu [b]

[a] Bahçeşehir University, Faculty of Engineering and Natural Sciences, Energy Systems Engineering Department, Beşiktaş, İstanbul 34353, Turkey
[b] Marmara University, Faculty of Engineering, Chemical Engineering Department, Maltepe, İstanbul 34854, Turkey

ARTICLE INFO

Keywords:
$NiFe_2O_4$
Photocatalytic H_2 production
TiO_2
Magnetic photocatalyst
Ag^+ doping

ABSTRACT

This work aims to design and develop a photocatalyst with the main three properties: *i)* reduced bandgap for solar activation of the photocatalyst, ii) retarded e^- / h^+ recombination rate for the enhanced photocatalytic activity, iii) magnetic separability from the reaction medium. In this study, $NiFe_2O_4/TiO_2$-Ag^+ photocatalysts were synthesized to modify the structural properties of TiO_2. Firstly, $NiFe_2O_4$ nanoparticles were synthesized by a conventional co-precipitation method, then in the presence of $NiFe_2O_4$ nanoparticles, TiO_2 was synthesized by a novel complex-assisted vapor thermal (VT) method via slow hydrolysis of Ti-complex. After the best wt% amount of $NiFe_2O_4$ in the $NiFe_2O_4/TiO_2$ had been determined for photocatalytic activity, Ag^+ was added by wet-impregnation. The photocatalysts were characterized by X-ray diffraction (XRD), UV–vis Diffuse Reflectance Spectroscopy (DRS), Photoluminescence Spectroscopy (PL), vibrating sample magnetometer analysis (VSM), transmission electronic microscopy (TEM), and X-ray photoelectron spectroscopy (XPS).

Photocatalytic hydrogen production reactions were carried out in methanol/water solution under solar light illumination. Consequently, the best configuration of the photocatalyst was determined as 12 wt% $NiFe_2O_4$/TiO_2-0.5 wt% Ag^+ (12NFT-0.50Ag^+) which had shown the maximum hydrogen (H_2) production rate as 137 μmol/g-cat after 5 h owing to its reduced bandgap energy and delayed e^- / h^+ recombination.

1. Introduction

Photocatalytic H_2 production via water splitting using semiconductors has had great attention since Fujishima and Honda studied photocatalytic degradation of water on TiO_2 [13]. TiO_2 is a primary semiconductor due to its long-term chemical stability against photo-corrosion, non-toxicity, high oxidizing power, etc. [27]. However, there are some limitations to using TiO_2 in photocatalytic applications. TiO_2 has a wide bandgap (3.2 eV for anatase, 3.0 eV for rutile), responding only to ultraviolet (UV) irradiation that corresponds to the wavelength of 390 nm for photoactivation. Solar light emission contains UV light as a small fraction (2–5%) while approximately half of it (42–47%) is visible light (390–750 nm) [22,58]. Thus solar irradiation response of TiO_2 should be enhanced by some modifications. Lots of studies have reported several types of additives like anions (N, P, etc.), metal oxides ($CuCr_2O_4$, NiO_x, etc.), metal sulfurs (CdS, $ZnIn_2S_4$, etc) to reduce the bandgap energy of TiO_2, thus the photoactivation under solar illumination obtained [53,54,50,30,41,55].

The photocatalytic reaction starts with the absorption of the light corresponding to the bandgap energy of TiO_2, and photo-excited electron-hole (e^-/ h^+) pairs form ($TiO_2 + h\nu \rightarrow e^-(CB) + h^+(VB)$). Another limitation causing the low photocatalytic activity is the recombination of these photo-excited e^- / h^+ pairs [26]. Therefore, TiO_2 needs modification to decrease the e^- / h^+ recombination rate [29]. Many studies have shown that metal ion doping to TiO_2, anion doping to TiO_2, or metal oxide modification of TiO_2 are effective ways to trap the photo-generated electron (e^-) and hole (h^+) separately and temporarily, thus suppressing the recombination of charge carriers [48,51,38].

Recently, modification of TiO_2 with magnetic spinel structured ferrite nanoparticles (MFe_2O_4) is an attractive field of study because MFe_2O_4 (M: Zn, Ni, Co, Ca, etc.) nanoparticles have a narrow bandgap to be a good sensitizer for wide bandgap semiconductors ($ZnFe_2O_4$: 1.9 eV, $NiFe_2O_4$: 1.56 eV, $CoFe_2O_4$: 1.10 eV, $CaFe_2O_4$: 1.85 eV) [58,37,39,36]. They have interesting properties such as several redox states,

* Corresponding author.
E-mail address: irem.firtina@eng.bau.edu.tr (I. Firtina-Ertis).

https://doi.org/10.1016/j.jphotochem.2022.114106
Received 7 April 2022; Received in revised form 7 June 2022; Accepted 18 June 2022
Available online 20 June 2022

appropriate band positions, thermal stability, low cost, and easy preparation [58]. Moreover, these magnetic nanoparticles address the problem of photocatalyst separation from the reaction medium [24]. For example, Chang et al. produced magnetically separable Fe_3O_4@ZnS and $NiCo_2O_4$@ZnS core–shell photocatalysts by the solvothermal method and recycled them for repeated hydrogen generation. They have found a good photocatalytic activity after being recycled three times [6]. Besides, Chang et al. also synthesized $CoFe_2O_4$@ZnS core–shell nanoparticles and then recycled them by applying magnetic force for hydrogen generation. They have seen that the photocatalytic activity was improved by calcination and recycling again after three times [7]. Thus, MFe_2O_4/TiO_2 photocatalysts have a high potential for photocatalytic applications and they incorporate the main three properties: i) reduced bandgap for solar activation of the photocatalyst, ii) retarded e^- / h^+ recombination rate for the enhanced photocatalytic activity, iii) magnetic separability from the reaction medium.

Many studies have been carried out with MFe_2O_4/TiO_2 photocatalysts for especially photocatalytic degradation of organic hazardous substances [39,58,56,9,31]. Also, for enhanced photocatalytic activity trio combination of TiO_2 based photocatalysts were studied. For example, Lu et al. synthesized $GO/NiFe_2O_4/TiO_2$ composite photocatalysts by hydrothermal method for degradation of unsymmetrical dimethylhydrazine from water under visible light. They have observed that electrons and holes excited from $NiFe_2O_4$ and well separated due to the band energy matching between $NiFe_2O_4$ and TiO_2 during degradation [31]. $TiO_2/Ag/NiFe_2O_4$ heterostructure prepared by co-precipitation of $NiFe_2O_4$ in the presence of commercial TiO_2 or commercial TiO_2-photo deposited Ag was reported [45]. Pd was used as a co-catalyst in TiO_2–$ZnFe_2O_4$, and this trio concept photocatalyst was prepared by sol–gel hydrolysis of Ti precursor in the presence of ferrite; after that Pd was loaded by impregnation [17]. But, there are limited numbers of reports for photocatalytic H_2 production with the usage of MFe_2O_4/TiO_2 synthesized by different methods. For example, $CaFe_2O_4/TiO_2$ photocatalysts were prepared by the solid-phase dispersion method and they were used for photocatalytic H_2 production from a methanol–water mixture [36]. Kezzim et al. studied visible light induced H_2 production by $CuFe_2O_4/TiO_2$ photocatalyst prepared by a modified sol–gel method in the presence of $CuFe_2O_4$ [23]. Also, for enhanced photocatalytic H_2 production as a trio concept photocatalyst, $CoFe_2O_4$–TiO_2/rGO synthesized by ultrasound-assisted wet impregnation method via mixing specific amounts of RGO, TiO_2, and $CoFe_2O_4$ starting from RGO suspension were studied [16]. Additionally, Ag photo deposited $CaFe_2O_4/TiO_2$ was studied by Reddy et al. [36]. It is well-known that noble metals like Pt, Au, Pd, and Ag demonstrate outstanding activity in photocatalytic reactions leading to serve as a charge trapper thus decreasing the e^- / h^+ recombination rate [26]. Thus, the synergistic effect of MFe_2O_4 and noble metal in trio concept modified versions of TiO_2 in photocatalytic H_2 production is found as worth the effort.

To sum up, semiconductor photocatalysts cannot show high photocatalytic activity alone because of their high recombination rate and it is necessary to construct a heterojunction structure as an interface between two semiconductors [28]. The design of heterojunction structure mainly focuses on two key points which are suitable band arrangement and the ideal interfaces for e^- / h^+ separation between semiconductors [12]. A conventional type-II heterojunction (Z-scheme) mechanism has been a good approximation, but it is not thermodynamically beneficial for photocatalytic oxidation and reduction reactions. There are limitations to the kinetics of the charge transfer mechanism because of Coulombic attraction forces [12]. Instead of type-II heterojunction mechanism (Z-scheme), a new step-scheme mechanism (S-scheme) has been proposed [12,28,57]. In S-scheme heterojunction mechanism, there is a construction between a reduction semiconductor and an oxidation semiconductor. The conduction band and Fermi level for the reduction semiconductor have higher than those of the oxidation semiconductor. Useless photo-generated holes of reduction semiconductor combined with the useless photogenerated electrons of oxidation semiconductor which are eliminated from the surface reactions. Adversely, useful holes of oxidation semiconductor and useful electrons of reduction semiconductor will participate the surface redox reaction [12,28]. Recently, there are several studies about S-scheme heterojunction photocatalysts such as the photocatalytic activity of step-scheme WO_3/TiO_2 for H_2 production [19], and step-scheme $LaNiO_3/TiO_2$ heterojunction with enhanced photocatalytic H_2 production activity [8].

Several methods have been used for the synthesis of $NiFe_2O_4/TiO_2$ such as mechanical mixing, solid-state dispersion, sol–gel, hydrothermal, etc. [36]. In this study, a novel complex assisted vapor thermal (VT) method, which is slow hydrolysis of Ti-triethanolamine (TEA) complex in the presence of $NiFe_2O_4$, was used to develop TiO_2-based modified photocatalysts ($NiFe_2O_4/TiO_2$-Ag^+). Different %wt amounts of $NiFe_2O_4$ and Ag^+ in the photocatalyst were investigated in terms of hydrogen production from methanol/water solution under solar light illumination. Besides, the relationship between the physical, optical, and electronic structure of the photocatalysts and hydrogen production was clarified and the best configuration of the photocatalyst was obtained.

2. Experimental procedure

2.1. Materials

All the reagents were used without further purification. Iron (III) nitrate nanohydrate ($Fe(NO_3)_3{\cdot}9H_2O$, Merck), nickel (II) nitrate hexahydrate ($Ni(NO_3)_2{\cdot}6H_2O$, Merck), PEG 20,000 (Merck), 25% NH_3 (Merck), titanium isopropoxide 97% ($Ti[OCH(CH_3)_2]_4$, TISOP, Sigma-Aldrich), triethanolamine ($C_6H_{15}NO_3$, TEA, Merck), 2-Propanol (C_3H_8O, Carlo Erba), silver nitrate ($AgNO_3$, Merck) were used as chemicals.

2.2. Preparation of $NiFe_2O_4$ (NF) nanoparticles

In a typical synthesis of MFe_2O_4, spinel structures were obtained by the coprecipitation method [46]. Ni^{2+} ($Ni(NO_3)_2{\cdot}6H_2O$) and Fe^{3+} (($Fe(NO_3)_3{\cdot}9H_2O$) salts were dissolved in deionized water with a 1:2 M ratio. 2 g of PEG 20,000 was added under magnetic stirring. The pH of the solution was adjusted to 11–12 under magnetic stirring and was kept at 70 °C for 2 h. The brownish precipitate was filtered, washed with deionized water several times, and then dried at 80 °C for 6 h. Then, the sample was homogenized by grinding in an agate mortar and the powder calcinated at 500 °C for 2 h to form magnetic $NiFe_2O_4$ nanoparticles.

2.3. Preparation of $NiFe_2O_4/TiO_2$ (NFT) by complex-assisted vapor thermal (VT) method

A novel complex-assisted vapor thermal (VT) method was applied to synthesize NFT magnetic photocatalysts. A specified amount of $NiFe_2O_4$ nanoparticles were dispersed in 5 ml 2-propanol, and 0.5 ml NH_3 %25 was added dropwise; the dispersion was kept in an ultrasonic bath for 30 min. Separately, TISOP with TEA solution was prepared in 2-propanol with the molar ratio of Ti: TEA = 1:2. The yellow transparent solution was kept under magnetic stirring for 30 min. A stable Ti-TEA complex was formed against fast hydrolysis of Ti^{4+} at room temperature [44]. Ti-TEA complex solution was added to $NiFe_2O_4$ dispersion dropwise when the dispersion was still in the ultrasonic bath. The mixture of $NiFe_2O_4$ dispersion and Ti-TEA complex was kept in an ultrasonic bath for 10 min more. This final mixture was taken to a PTFE vessel; the vessel was placed in a water bath in the stainless steel autoclave to perform the vapor-thermal method. The stainless steel autoclave was retained at 160℃ for 24 h; thus the complex-assisted VT method was applied via the slow hydrolysis reaction of the Ti-TEA complex by vapor inside the autoclave. After 24 h, the autoclave was cooled down to room temperature naturally; precipitation was filtered,

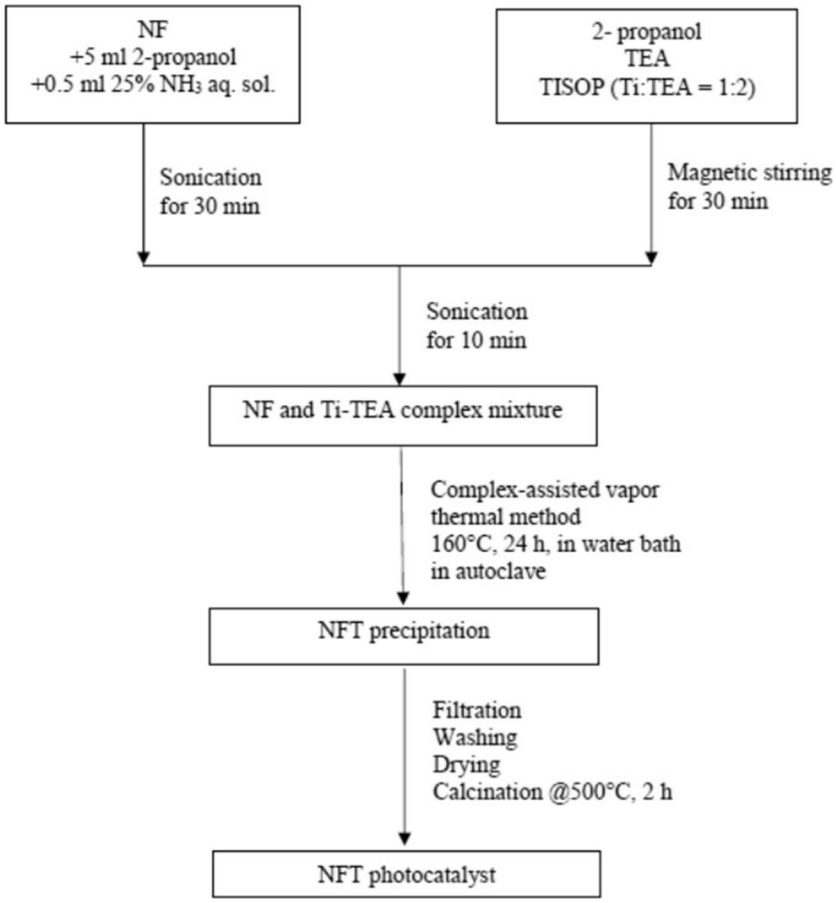

Fig. 1. Schematic flow diagram for the preparation of $NiFe_2O_4/TiO_2$ (NFT) by complex-assisted vapor thermal (VT) method.

washed with 2-propanol, and then dried at 80 °C for 2 h. The powder was calcinated at 500 °C for 2 h to form magnetic $NiFe_2O_4/TiO_2$ (NFT) as illustrated in Fig. 1.

The procedure was repeated with the different amounts of $NiFe_2O_4$ nanoparticles by weight (wt) % of the whole $NiFe_2O_4/TiO_2$ and named 4NFT, 8NFT, 12NFT, 20NFT. Ag^+ doped $NiFe_2O_4/TiO_2$ (NFT) nanoparticles were obtained by the wet impregnation method. Specific concentrations of aqueous $AgNO_3$ solution were prepared and impregnated on 12NFT. The samples were dried at 100 °C for 4 h. Different Ag^+ amounts were prepared by wt% as follows: 12NFT-0.10Ag^+, 12NFT-0.25Ag^+, 12NFT-0.50Ag^+, 12NFT-1.00Ag^+, 12NFT-2.50Ag^+.

2.4. Characterization

NFT nanoparticles were characterized by X-ray diffraction (XRD) using Rigaku D/Max-2200 diffractometer with CuKα (λ = 1.5405) radiation. Samples were scanned from 10° to 80° at a rate of 2°/min (in 2θ). The UV–vis DRS of the samples in the wavelength range 200–800 nm were obtained by PG instrument T92 + spectrophotometer by using $BaSO_4$ as reference. Magnetic properties were characterized by a vibrating sample magnetometer (Cryogenic Limited PPMS) at room temperature. Photoluminescence spectroscopy (PL, DongWoo Optron) was used to examine e^-/ h^+ recombination rates. Transmission electronic microscopy (TEM) analyses were conducted with a Hitachi HighTech HT7700 electron microscope (40–120 kV). X-ray photoelectron spectroscopy (XPS, Specs-Flex) was used to determine the binding energies and the chemical composition of a synthesized photocatalyst.

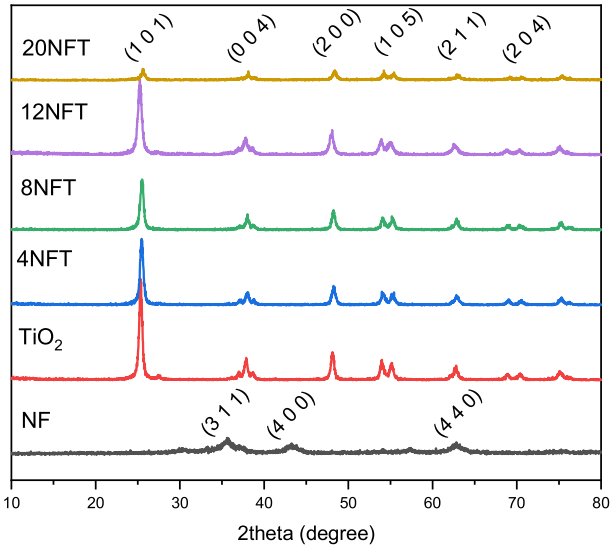

Fig. 2. The XRD patterns of NF, TiO_2, and NFT with different wt% of NF.

2.5. Photocatalytic experiments

Photocatalytic hydrogen production reactions were carried out in a homemade quartz based reactor. In all experiments, 2.5 g/L photocatalyst and 50:50% (v:v) methanol/water solution were used. HAL-320 Compact Xenon Light Source Solar Simulator was used to simulate sunlight, and the distance between the photocatalyst and the light

Table 1
Crystallite size of the NFT photocatalysts.

Photocatalyst	D (nm)
TiO_2	17.8
4NFT	16.4
8NFT	16.0
12NFT	13.9
20NFT	15.7

source was adjusted to obtain the light intensity as 1000 Wm^{-2}. The amount of gas evolved was measured using a water manometer. The gas collected from the outlet of the reactor was analyzed by GC (Agilent 6890); H_2 was qualitatively recognized.

3. Results and discussion

3.1. Structural analysis

3.1.1. X-ray powder diffraction (XRD)

X-ray powder diffraction (XRD) was performed to investigate the structure and the average crystallite size of the photocatalysts. Fig. 2 shows X-ray diffraction (XRD) patterns of TiO_2 photocatalysts containing NF in different weight percentages (wt%) prepared by the complex-assisted vapor-thermal (VT) method. Besides, the XRD patterns of NF and TiO_2 samples are given in Fig. 2. The characteristic peaks of $NiFe_2O_4$ indicated a crystal spinel structure was observed at 30.29°, 35.70°, 37.31°, 43.36°, 53.80°, 57.36°, and 62.92° which were assigned to the (220), (311), (222), (400), (422), (511) and (440) planes, respectively (JCPDS No 54-0964) [32,18]. The characteristic peaks of TiO_2 indicated anatase structure were observed at 25.24°, 37.08°, 37.91°, 38.65°, 48.10°, 53.97°, 55.07°, and 62.87° which were assigned to the (101), (103), (004), (112), (200), (105), (211) and (204) planes, respectively (JCPDS No. 21-1272) [4]. Very low peak intensity was observed at $2\theta = 27.52°$ corresponding to the (110) plane of the rutile phase of TiO_2. NFT magnetic photocatalysts did not exhibit NF peaks, indicating only characteristic peaks of TiO_2 in the XRD patterns due to the low %wt amount of NF. However, the intensity of the peak at $2\theta = 25.24°$ of the anatase phase of TiO_2 was decreased and the peak was broader than the TiO_2 when the wt% amounts of NF in the magnetic photocatalyst was increased. Additionally, there is a peak shift for 20 NFT photocatalyst due to the high amount of NF relative to the others. Thus, it was observed that NFT photocatalysts have been successfully synthesized. Furthermore, there were no other peaks rather than NF and TiO_2.

The crystallite sizes were calculated using the Debye Scherrer's equation (Eq. (1)).

$$D = 0.9\lambda/\beta cos\theta \quad (1)$$

where λ is the wavelength of incident X-rays, β is full width at half maximum height in radians taken from the anatase peak at $2\theta = 25.24°$, and the θ is the diffraction angle [24]. Also, it has been well known that peak broadening shows a reduction in crystallite size. Generally, the main peaks of NFT with higher wt% amounts of NF were broader than the peaks of the bare TiO_2. However, 12NFT photocatalyst reached the lowest crystallite size (13.9 nm) among the photocatalysts as seen in Table 1. Thus, the crystallite size was increased again by dopping NF higher than 12 wt%. In parallel to this, 12NFT photocatalyst has shown the highest activity in hydrogen production under solar light illumination.

3.2. Morphological Analysis:

3.2.1. Transmission electron microscopy (TEM)

TEM analysis were used to determine its microstructure and morphology. Fig. 3 and Fig. 4 show the TEM images and the elementel mapping of the 12NFT-0.5Ag^+ photocatalyst, respectively. It was observed that NF and TiO_2 nanoparticles are in a homogeneous structure with diameters below 25 nm which is consistent with XRD results. As a result of the elementel mapping, the Ag element (in yellow color) in the magnetic photocatalyst could be detected.

3.3. Optical and magnetical analysis

3.3.1. UV–vis absorbance

UV–vis absorbance spectrum was used to demonstrate the optical absorption properties of the photocatalysts. The bandgap energy of the semiconductors is related to absorption wavelength, where a higher wavelength shows a lower band gap value. Tauc Plot which is the curve between photon energy (hν) and $[h\nu f(R)]^2$ is a good approximation to determine the bandgap energy of the photocatalysts by drawing a tangent to the curve and finding the interception point on the x-axis [40,42].

Fig. 5 shows the UV–vis absorbance spectra (a-b) and Tauc plots (c-d) of NFT with different wt% of NF and 12NFT with different wt% of Ag^+. The direct bandgap energy of the samples was calculated from Tauc plots by using the following equation (Eq. (2)):

$$(h\nu\alpha)^{1/n} = A(h\nu - E_g) \quad (2)$$

where E_g is the band gap energy, h is Planck's constant, v is the frequency of vibration, hv is the photon energy, A is a proportional constant and α is the absorption coefficient. The absorbance or Kubelka–Munk function of the reflectance (f(R)) is proportional to the absorption coefficient, α [25,49]. The direct allowed transition is used in this experiment, $n = 1/2$ is used for the samples. Bandgap energy of the synthesized TiO_2, 4 wt% $NiFe_2O_4/TiO_2$ (4NFT), 8 wt% $NiFe_2O_4/TiO_2$

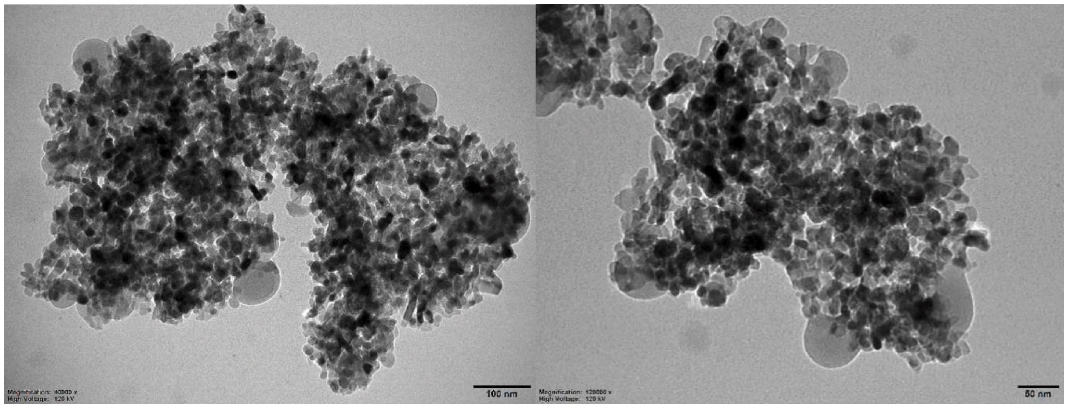

Fig. 3. TEM images of 12NFT-0.5Ag^+ photocatalyst.

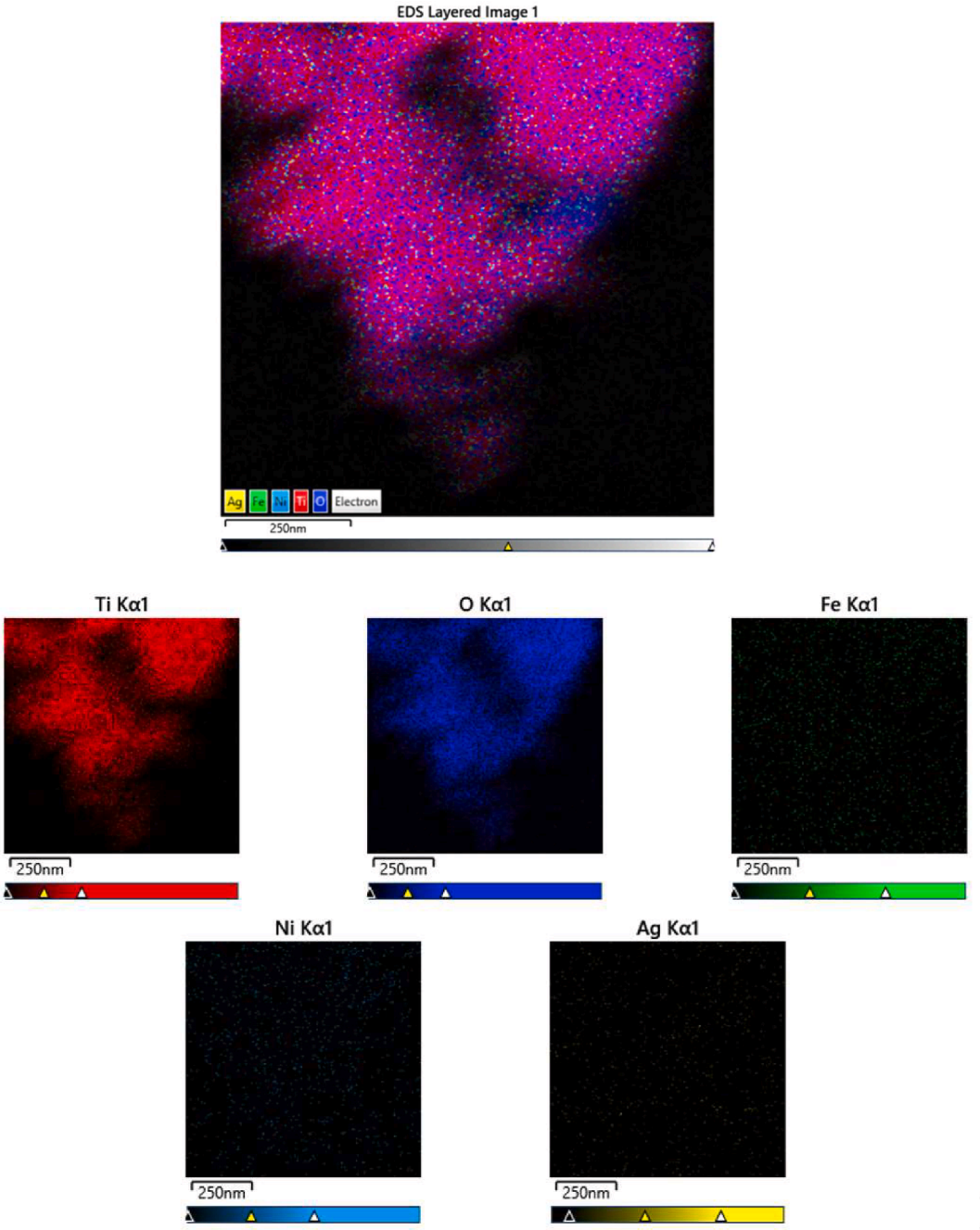

Fig. 4. TEM elementel mapping of 12NFT-0.5Ag^{+} photocatalyst.

(8NFT), 12 wt% $NiFe_2O_4/TiO_2$ (12NFT), 20 wt% $NiFe_2O_4/TiO_2$ (20NFT) photocatalysts were calculated as 3.28 eV, 3.19 eV, 3.01 eV, 2.94 eV, and 2.87 eV indicated in Table 2, respectively.

In Fig. 5(a) and 5(c), the absorption band corresponding to the octahedral symmetry of Ti^{4+} was present between 350 and 380 nm, indicating a band gap of 3.2 eV [24]. Besides, it was observed that as the wt% of NF in the photocatalyst increased, the absorbance in the visible area slightly increased. Not only the bandgap energy change by adding NF but also decreased below 3.00 eV by modifying the photocatalyst with Ag^{+} as seen in Fig. 5(b) and 5(d). 12NFT magnetic photocatalyst indicated a bandgap of 2.94 eV whereas 12NFT-0.5Ag^{+} photocatalyst had 2.71 eV bandgap energy. Therefore, it was observed that the bandgap energy of the photocatalyst was affected by increasing wt% of NF and Ag^{+} doping [34].

3.3.2. *Photoluminescence*

The photoluminescence properties and the electron-hole (e^{-}/h^{+}) recombination behavior of the photocatalysts were analyzed by photoluminescence (PL) spectroscopy. It presents that the electrons in the valence band are transferred to the conduction band, and then return to the valence band by photoemission. When the e^{-} / h^{+} recombination rate is slow, PL intensity decreases, and thus, this will result in enhanced photocatalytic hydrogen production [36].

PL spectrum was also used to identify the defective regions by peak deconvolution. Fig. 6 (a) shows the deconvoluted PL spectrum of TiO_2 where the centers at 496 nm, 541 nm, 621 nm, and 649 nm are matched coherently with four Gaussian peaks (P1-P4). These emission bands were existed due to three different physical situations: i) self-trapped excitons, ii) oxygen vacancies, and iii) surface states [10].

Fig. 6 (b) shows the PL spectra of NFT with different wt% of NF and

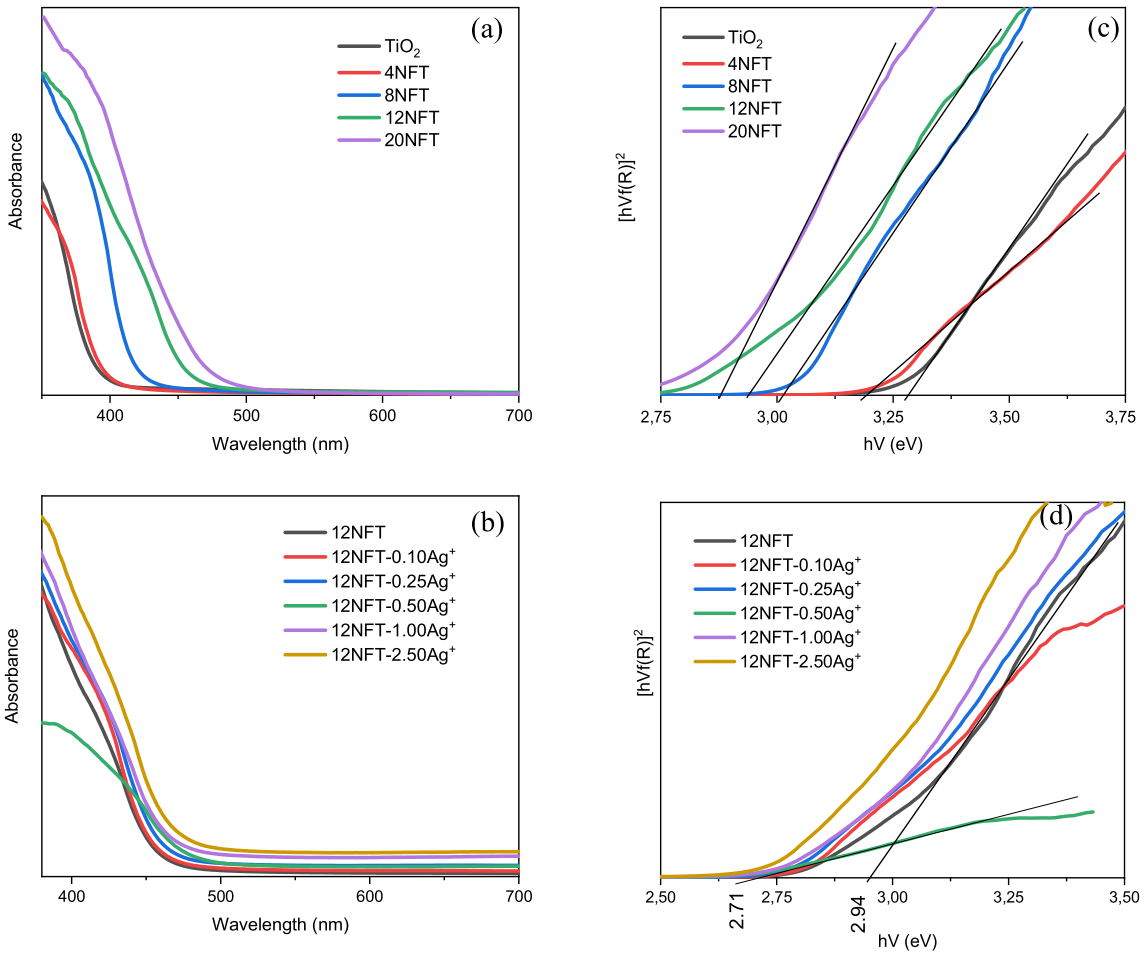

Fig. 5. UV–vis absorbance spectrum of **(a)** NFT with different wt% of NF **(b)** 12NFT photocatalyst with different wt% of Ag^{+}. Tauc plots for **(c)** NFT with different wt % amounts of NF **(d)** 12NFT photocatalyst with different wt% of Ag^{+}.

Table 2
Bandgap energies of the photocatalysts.

Photocatalyst	Bandgap (eV)	Photocatalyst	Bandgap (eV)
TiO_2	3.28	12NFT-0.10 Ag^{+}	2.84
4NFT	3.19	12NFT-0.25 Ag^{+}	2.84
8NFT	3.01	12NFT-0.50 Ag^{+}	2.71
12NFT	2.94	12NFT-1.00 Ag^{+}	2.86
20NFT	2.87	12NFT-2.50 Ag^{+}	2.82

Fig. 6 (c) shows the PL spectra of 12NFT with different wt% of Ag^{+}. PL intensity was substantially quenched by adding NF. This reveals that e^{-} / h^{+} recombination was reduced and it was supported by the increase in photocatalytic activity as well as magnetically separable property due to the existence of NF. Thus, NF plays a vital role to prevent the recombination of e^{-} / h^{+} pairs which is the reason for the improved photocatalytic activity of NFT. The secondary peak was also observed between 600 and 700 nm as shown in Fig. 6(b) and (c) which is proof of NF existence in the photocatalyst [43]. Besides, the PL intensity was decreased by adding Ag^{+} on the 12NFT surface as seen in Fig. 6(c).

In Fig. 6(c), the PL intensity of 12NFT-0.50Ag^{+} photocatalyst was lesser than 12NFT, which illustrated that the recombination process was much slower in 12NFT-0.50Ag^{+}. When Ag^{+} %wt amount in the photocatalyst increases, the PL intensity decreases. However, 12NFT-2.50Ag^{+} shows low photocatalytic activity in H_2 production reaction due to its wider bandgap relative to 12NFT-0.50Ag^{+}.

3.3.3. *Magnetical analysis*

Fig. 7 shows the magnetic hysteresis cycles that are characteristic of ferromagnetism as a result of VSM analysis for NFT with different wt% of NF. It was naturally observed that the intensity of magnetic separation was increased by increasing the wt% of NF in the photocatalyst. Thus, these nanoparticles can be separated from methanol/water solution when an external magnetic field is applied, and they can be dispersed into the solution again after the external magnetic field is removed [47].

3.3.4. *X-ray photon spectroscopy (XPS)*

12NFT-0.5 Ag^{+} was examined before and after hydrogen production reaction by X-ray photon spectroscopy (XPS) to determine the binding energies and the chemical composition. The results indicated that the photocatalyst contained Ti, Fe, Ni, and Ag in Fig. 8. It is well known that the anatase TiO_2 has binding energies of 458.2 eV and 463.9 which corresponds to the $Ti2p_{3/2}$ and $Ti2p_{1/2}$ spin-orbital splitting photoelectrons, respectively [15] and indicates the presence of Ti^{4+} [24]. In this study, bands were almost at the same binding energies of 458.2 and 464.0 eV for $Ti2p_{3/2}$ and $Ti2p_{1/2}$, respectively. Besides, the bands remained significantly unchanged after hydrogen production, with the binding energies corresponding to Ti^{4+}, with no Ti^{3+} impurities in the photocatalyst, indicating that the anatase structure was not altered even at the surface during the synthesis of the binary or ternary structure (Fig. 8(a)).

The binding energies of 711.7 eV and 727.4 eV corresponding to $Fe2p_{3/2}$ and $Fe2p_{1/2}$ in the photocatalyst were slightly shifted to higher energy as compared with the literature (710.0 and 724.0 eV for Fe_3O_4), respectively [24], indicating a higher Fe oxidation state in the

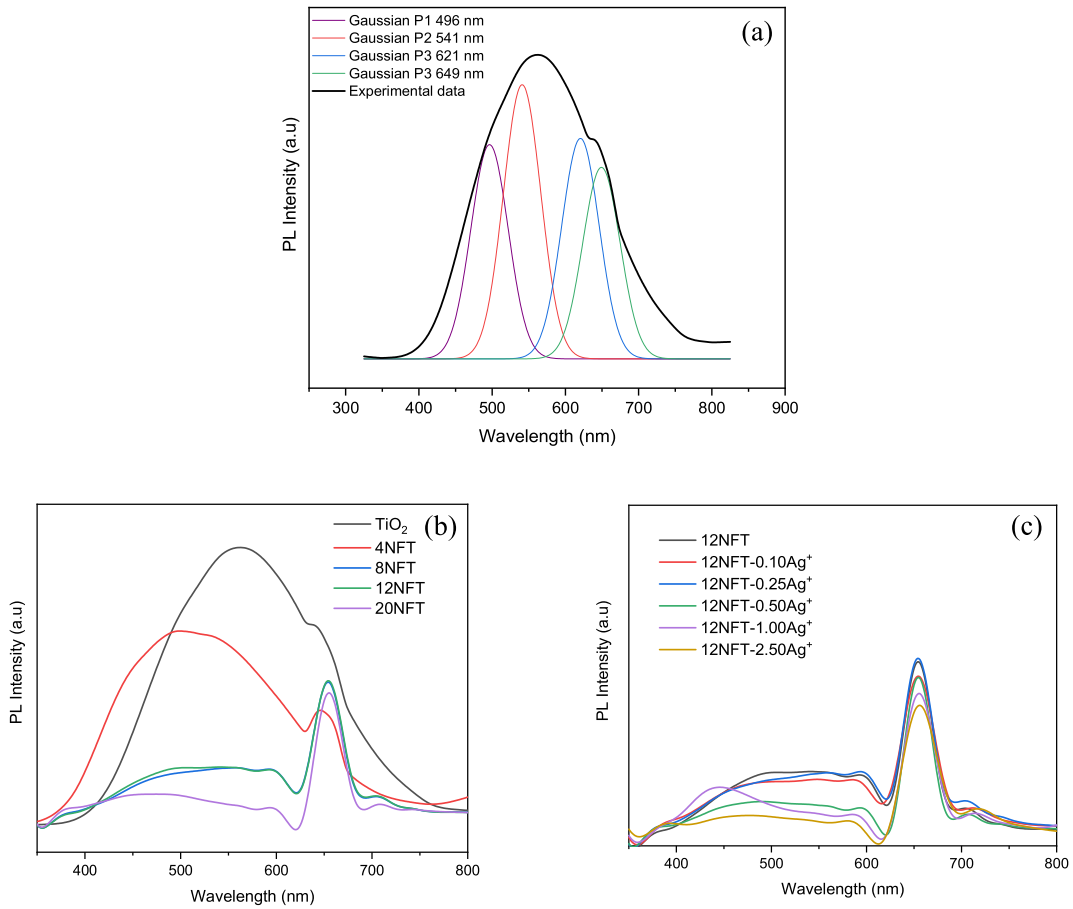

Fig. 6. Photoluminescence (PL) spectrum of **(a)** deconvoluted Gaussian peaks of TiO_2 **(b)** NFT with different wt% of NF **(c)** 12 NFT photocatalyst with different wt% of $Ag^{+.}$

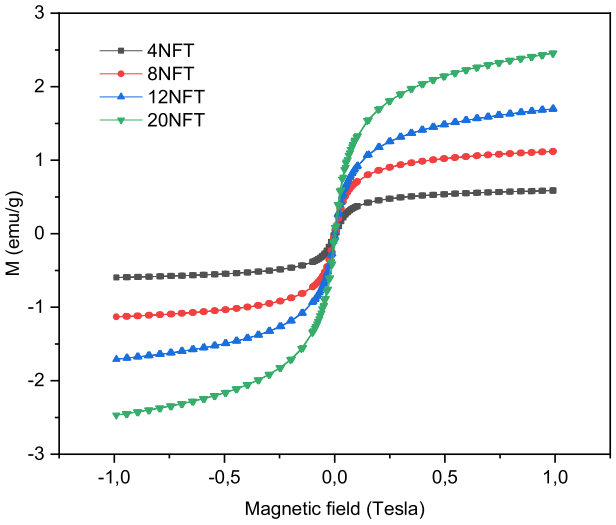

Fig. 7. Vibrating-sample magnetometer (VSM) analysis for NFT with different wt% of NF.

photocatalyst. However, the $Fe2p_{3/2}$ and $Fe2p_{1/2}$ bands shifted to lower energy, 709.6 eV and 722.6 eV, respectively after hydrogen production [45], indicating that Fe ions in the photocatalyst were reduced from Fe^{3+} to Fe^{2+} (Fig. 8(b)).

Fig. 8(c) shows that Ni2p has binding energies of 874.2 eV and 854.1 eV indexed to $Ni2p_{1/2}$ and $Ni2p_{3/2}$ before the H_2 reaction, respectively. The binding energies of 874.6 eV and 873.5 eV were attributed to the tetrahedral (T_d) environment and octahedral (O_h) environment of $Ni2p_{1/2}$ whereas the binding energies of 856.6 eV and 855.5 eV were attributed to the T_d environment and O_h environment of $Ni2p_{3/2}$, respectively [11,24]. Regarding this, the peaks located at binding energies of 874.2 eV and 854.1 eV (Fig. 8(c)) can be attributed to the tetrahedral (T_d) environment of $Ni2p_{1/2}$ and the octahedral (O_h) environment of $Ni2p_{3/2}$, respectively. After the H_2 production reaction, the binding energy of $Ni2p_{3/2}$ at 854.1 nm shifted to 856.6 eV indicating that Ni^{2+} is mainly coordinated with oxygen in a form of an octahedral structure [45].

Ag3d has binding energies of $Ag3d_{5/2}$ and $Ag3d_{3/2}$ corresponding to 367.2 eV and 373.1 eV before the H_2 reaction, respectively, as seen in Fig. 8(d). These values were not clear to distinguish between the different chemical states of Ag, as it is known that the Ag3d binding energy of 368.2 eV for metallic silver (Ag), 367.8 eV for Ag_2O (Ag^+) and 367.4 eV for AgO (Ag^{2+}), and corresponding to $Ag3d_{5/2}$ and 374.2 eV, 373.8 eV and 373.2 eV corresponding to $Ag3d_{3/2}$, respectively [1,2,45]. As the binding energy shifts to lower values, the oxidation state of silver changes in the order of Ag, Ag^+, and Ag^{2+}. Notably, the $Ag3d_{5/2}$ and $Ag3d_{3/2}$ binding energies shifted from 367.6 to 366.5 eV and 373.1 to 372.6 eV, respectively (Fig. 8(d)), where it was observed that the XPS spectra of Ag3d showed Ag^+ and Ag^{2+} in the synthesized photocatalyst before and after H_2 production reaction, respectively. Regarding this, it can be concluded that Ag^+ particles play a significant role in effective e^-/h^+ separation by trapping holes thereby increasing the photocatalytic activity.

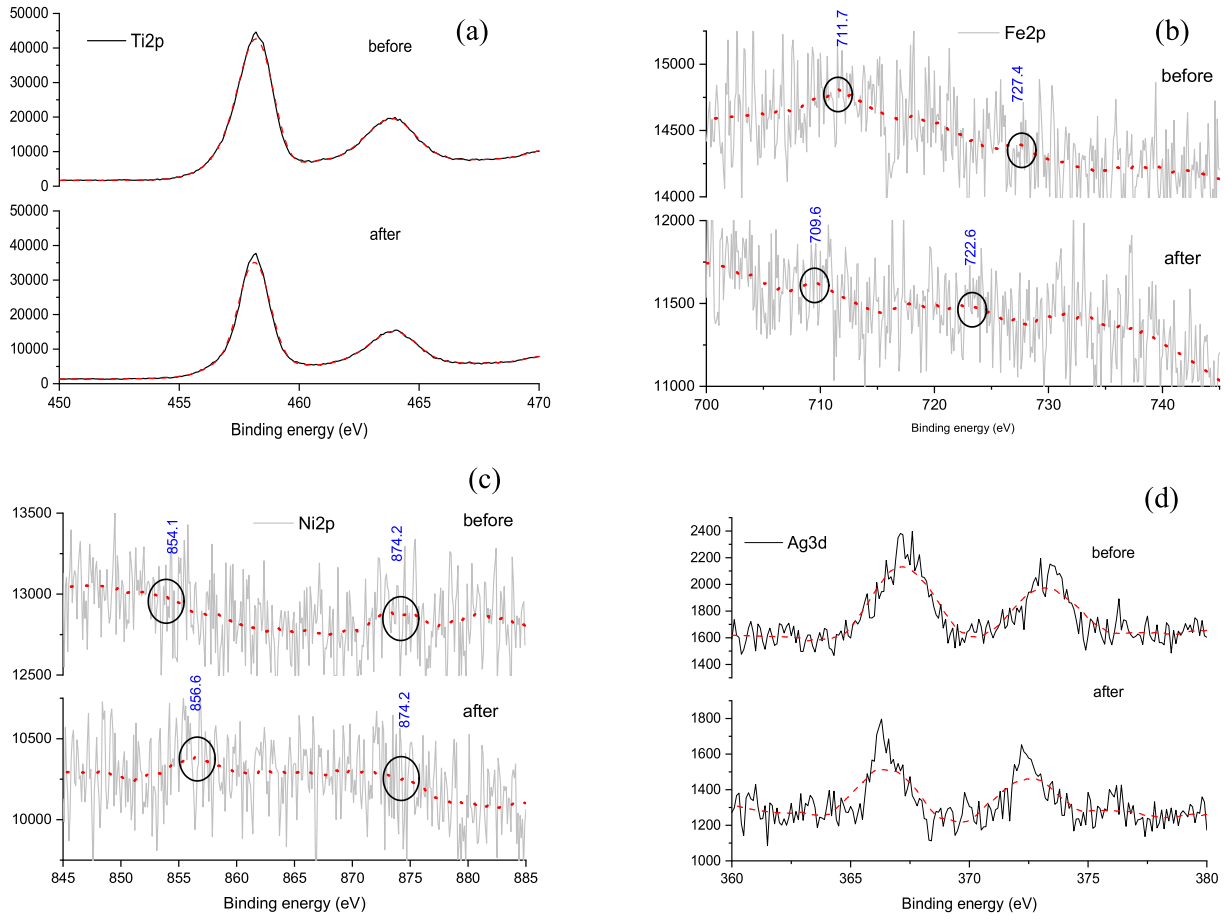

Fig. 8. The XPS spectra of Ti2p (a), Fe2p (b), Ni2p (c) and Ag3d (d) in the photocatalyst before and after hydrogen production reaction.

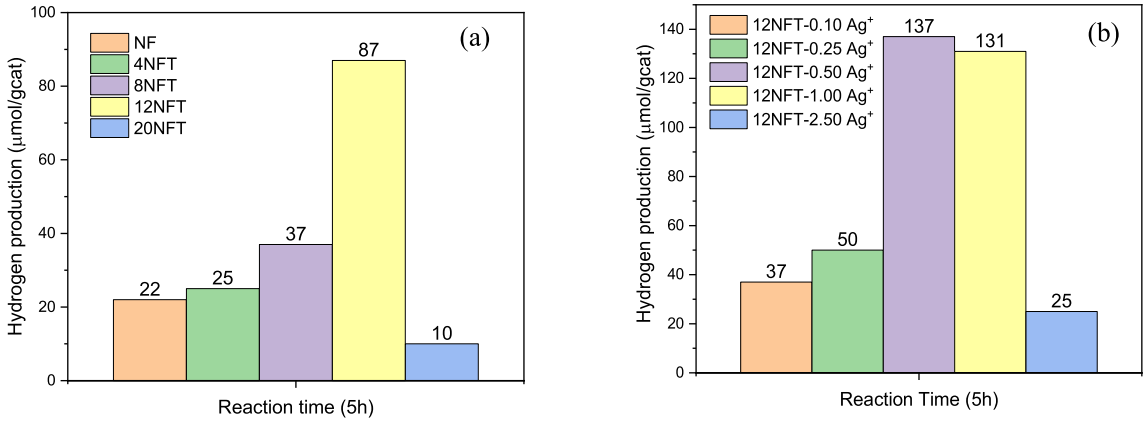

Fig. 9. H_2 production from the photocatalytic splitting of methanol/water solution over (a) NF and NFT photocatalysts with different wt% of NF (b) 12NFT photocatalyst with different wt% of Ag^+ under solar light illumination.

3.4. Photocatalytic activity measurement

Photocatalytic activity on NF, NFT, and 12NFT with different wt% of Ag^+ was evaluated for hydrogen production from methanol/water solution under solar light illumination (Fig. 9). Hydrogen production was not observed on bare TiO_2 under solar light whereas, 22 μmole/gcat was observed on bare NF. 12NFT showed the highest photocatalytic activity i.e., 87 μmole/gcat among the NFT photocatalysts. Besides, 12NFT reached the highest amount of H_2 by doping 0.5 wt% Ag^+ as 137 μmol/g-cat among all the magnetic photocatalysts.

Generally, better crystallinity, low crystallite size, narrow bandgap, and low PL intensity of a photocatalyst play a major role in efficient charge separation and high photocatalytic activity. In this study, the reasons for better activity of NFT may be due to i) fine dispersion of NF over the TiO_2 ii) low crystallite size of 12NFT photocatalyst iii) Ag^+ deposition on the 12NFT surface provides narrow band gap and play a role in hole sinks as active sites for proton reduction to decrease e^- / h^+ recombination iv) low PL intensity of 12NFT and also 12NFT-0.50Ag^+ (Fig. 6) that make charge separation more facile thereby increasing the production of H_2 [36]. The amount of hydrogen generated after 5 h of photocatalytic reaction increased in the order of 12NFT-0.50 Ag^+ >12NFT-1.00 Ag^+ >12NFT-0.25 Ag^+ >12NFT-0.10 Ag^+ >12NFT-2.50

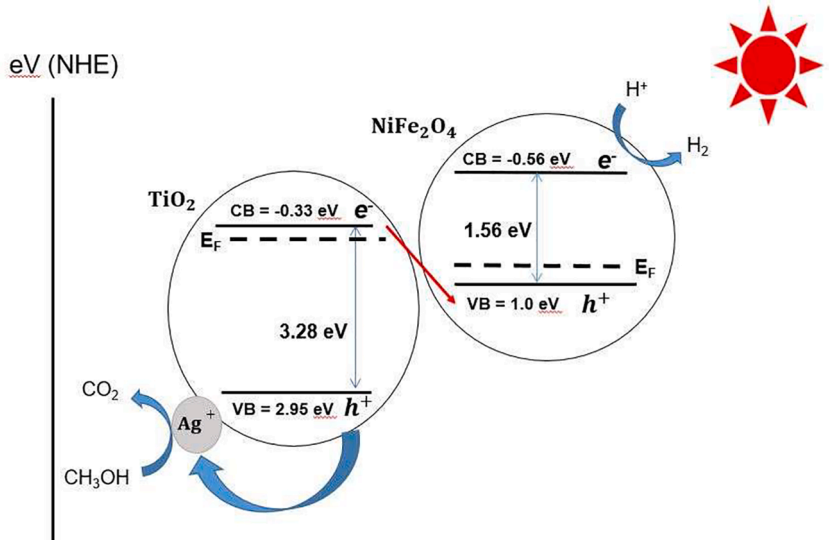

Fig. 10. The S-scheme representation of electron-hole transfer for $NiFe_2O_4/TiO_2$-Ag^+ photocatalyst under solar light illumination.

Ag^+.

The general photocatalytic mechanism involves the following steps:

(a) Charge carrier generation: When photon energy is absorbed by a TiO_2 particle, an e^- / h^+ pair is generated. The e^- and h^+ may migrate to the surface of the photocatalyst particle and react with adsorbed reactants.

$$TiO_2 + h\nu \rightarrow h^+(VB) + e^-(CB) \quad (3)$$

$$NiFe_2O_4 + h\nu \rightarrow h^+(VB) + e^-(CB) \quad (4)$$

(b) Production of hydroxyl radicals: At the TiO_2 particle surface, the holes may react with surface hydroxyl groups (OH^-) and adsorbed H_2O, to form $\dot{O}H$ radicals.

$$H_2O + h^+(TiO_2) \rightarrow \dot{O}H + H^+ + TiO_2 \quad (5)$$

(c) Recombination reaction: In the absence of electron or hole acceptors, electron-hole recombination is possible.

$$h^+(TiO_2) + e^-(TiO_2) \rightarrow TiO_2 + heat \quad (6)$$

(d) Production of superoxide ions: At the TiO_2 particle surface, the electrons can react with O_2 adsorbed through the formation of superoxide ions ($\dot{O}_2^-$).

$$O_2 + e^-(TiO_2) \rightarrow \dot{O}_2^- + TiO_2 \quad (7)$$

(e) Surface trapping: The doping agents can act as charge separators of the photoinduced e^-/h^+ pair thus enhancing the photocatalytic activity. Ferric ion (Fe^{3+}) was found to be an effective ion in $Ni^{2+}Fe_2^{3+}O_4$ because it serves as trapping sites for e^- (Fe^{3+}/Fe^{2+}) [35] and Ag_2^+O was served as a trapping site for h^+ ($Ag_2^+O/Ag^{2+}O$).

$$Fe^{3+} + e^- \rightarrow Fe^{2+} \quad (8)$$

$$Ag_2^+O + h^+ \rightarrow Ag^{2+}O \quad (9)$$

(f) Interfacial charge transfer:

$$CH_3OH + \dot{O}H \rightarrow \dot{C}H_2OH + H_2O \quad (10)$$

$$\dot{C}H_2OH + \dot{O}_2^- \rightarrow HCHO + H\dot{O}_2 \quad (11)$$

$$HCHO + H_2O \rightarrow HCOOH + H_2 \quad (12)$$

$$HCOOH \rightarrow CO_2 + H_2 \quad (13)$$

The photocatalytic activity is determined by the number of photogenerated charge carriers which can avoid the recombination reaction by considering the entire photocatalytic process. In this sense, the production of H_2 from methanol is directly related to the production of hydroxyl radicals, $\dot{O}H$, which play a vital role in photocatalysis. Thus, the resulting $\dot{O}_2^-$ and $\dot{O}H$ are very strong oxidizing agents that can convert methanol (CH_3OH) to formaldehyde (HCHO) then CO_2 and H_2 [3,52,21].

As shown in Fig. 10, TiO_2 and $NiFe_2O_4$ simultaneously generate electron-hole (e^- / h^+) pairs under solar light irradiation. There will be an internal electric field from $NiFe_2O_4$ to TiO_2. According to recently reported S-scheme heterojunction, the electrons on the CB of TiO_2 combined with the holes on the VB of $NiFe_2O_4$. The holes on the surface of the VB of TiO_2 react with the sacrificial agent via Ag^+. At the same time, the electrons on the CB of $NiFe_2O_4$ combine with H^+ to generate H_2 [12,57,28]. The band positions for TiO_2 and $NiFe_2O_4$ were obtained from reported literature [33,20,5,14].

4. Conclusion

In the study, NFT photocatalysts were synthesized by a novel complex assisted VT method with different %wt NF and Ag^+ nanoparticles. The results show that; the 12NFT photocatalyst which has reached the lowest crystallite size among the photocatalysts has shown the highest activity in hydrogen production; NFT absorption in the visible area slightly increased when wt% of NF in the photocatalyst increased; 12NFT magnetic photocatalyst indicated a bandgap of 2.94 eV whereas 12NFT-0.50Ag^+ modified photocatalyst had 2.71 eV bandgap energy; PL intensity was decreased by adding NF to TiO_2 and Ag^+ to NFT photocatalyst which reduced the rate of e^- / h^+ recombination; the intensity of magnetic separation was increased by increasing the wt% of NF in the photocatalyst; XPS spectra showed that ferric ion (Fe^{3+}) in $Ni^{2+}Fe_2^{3+}O_4$ and Ag_2^+O in the photocatalyst were served as trapping sites for e^- (Fe^{3+}/Fe^{2+}) and h^+ ($Ag_2^+O/Ag^{2+}O$), respectively.

Consequently, 12NFT-0.50Ag^+ is considered a promising photocatalyst due to better contact between NF and TiO_2 by using a novel complex-assisted VT method with the best configuration reaching the highest amount of H_2 as 137 μmol/g-cat whereas 12NFT produced 87.4 μmol/g-cat H_2 among the magnetic photocatalysts under solar light illumination.

CRediT authorship contribution statement

İrem Firtina-Ertis: Writing – original draft, Resources, Methodology, Investigation, Conceptualization. **Özge Kerkez-Kuyumcu:** Writing – review & editing, Visualization, Resources, Methodology, Conceptualization.

Declaration of Competing Interest

The authors declare that they have no known competing financial interests or personal relationships that could have appeared to influence the work reported in this paper.

Data availability

The authors do not have permission to share data.

Acknowledgment

This work was supported by TUBITAK with project number 216M386.

References

[1] I.M. Arabatzis, T. Stergiopoulos, M.C. Bernard, D. Labou, S.G. Neophytides, P. Falaras, Silver-modified titanium dioxide thin films for efficient photodegradation of methyl orange, Appl. Catal. B 42 (2003) 187–201.
[2] O.G. Ashkhotova, S.A. Khubezhov, M.A. Aleroev, T.T. Magkoev, G.S. Grigorkina, Effect of bombardment with oxygen ions on the surface composition of polycrystalline silver, Russ. J. Phys. Chem. A 92 (7) (2018) 1382–1385.
[3] A. Azizi, J. Saien, Optimization of Cr(VI) photocatalytic reduction by UV/TiO2: influence of inorganic and organic species and kinetic study, Arch Hyg Sci 7 (2) (2018) 81–90.
[4] S. Bakardjieva, J. Subrt, V. Stengl, M.J. Dianez, M.J. Sayagues, Photoactivity of anatase–rutile TiO_2 nanocrystalline mixtures obtained by heat treatment of homogeneously precipitated anatase, Appl. Catal. B 58 (2005) 193–202.
[5] S. Chandrasekaran, C. Bowen, P. Zhang, Z. Li, Q. Yuan, X. Ren, L. Deng, Spinel photocatalysts for environmental remediation, hydrogen generation, CO2 reduction and photoelectrochemical water splitting, J. Mater. Chem. A 6 (2018) 11078.
[6] C.J. Chang, Z. Lee, M.D. Wei, C.C. Chang, K.W. Chu, Photocatalytic hydrogen production by magnetically separable Fe3O4@ ZnS and NiCo2O4@ ZnS core-shell nanoparticles, Int. J. Hydrogen Energy 40 (35) (2015) 11436–11443.
[7] C.J. Chang, Z. Lee, K.W. Chu, Y.H. Wei, CoFe2O4@ ZnS core-shell spheres as magnetically recyclable photocatalysts for hydrogen production, J. Taiwan Inst. Chem. Eng. 66 (2016) 386–393.
[8] C. Chen, J.L. Zhou, J.F. Geng, R.Y. Bao, Z.H. Wang, J.X. Xia, H. Li, Perovskite LaNiO3/TiO2 step-scheme heterojunction with enhanced photocatalytic activity, Appl Surf Sci 503 (2020), 144287.
[9] P. Cheng, C. Deng, M. Gu, W. Shangguan, Visible-light responsive zinc ferrite doped titania photocatalyst for methyl orange degradation, J Mater Sci 42 (2007) 9239–9244.
[10] L. Chetibi, T. Busko, N.P. Kulish, D. Hamana, S. Chaieb, S. Achour, Photoluminescence properties of TiO2 nanofibers, J. Nanopart. Res. 19 (2017) 129.
[11] Z. Duan, Y. Zhu, Z. Hub, J. Zhang, D. Liu, X. Luo, M. Gao, L. Lei, X. Wanga, G. Zhao, Micro-patterned $NiFe_2O_4$/Fe–TiO_2 composite films: Fabrication, hydrophilicity and application in visible-light-driven photocatalysis, Ceram. Int. 46 (2020) 27080–27091.
[12] J. Fu, Q. Xu, J. Low, C. Jiang, J. Yu, Ultrathin 2D/2D WO3/g-C3N4 step-scheme H2-production photocatalyst, Appl. Catal. B 243 (2019) 556–565.
[13] A. Fujishima, K. Honda, Electrochemical photolysis of water at a semiconductor electrode, Nature 238 (1972) 37–38.
[14] C. Gao, J. Li, Z. Shan, F. Huang, H. Shen, Preparation and visible-light photocatalytic activity of In2S3/TiO2 composite, Mater. Chem. Phys. 122 (2010) 183–187.
[15] L.X. Ge, H. Fang, M. Sun, Preparation of TiO_2 thin films from autoclaved sol containing needle-like anatase crystals, Appl. Surf. Sci. 253 (2) (2006) 720–725.
[16] H.Y. Hafeez, S.K. Lakhera, N. Narayanan, S. Harish, Y. Hayakawa, B.K. Lee, B. Neppolian, Environmentally sustainable synthesis of a CoFe2O4–TiO2/rGO ternary photocatalyst: a highly efficient and stable photocatalyst for high production of hydrogen (solar fuel), ACS Omega 4 (1) (2019) 880–891.
[17] P.P. Hankare, R.P. Patil, A.V. Jadhav, K.M. Garadkar, R. Sasikala, Enhanced photocatalytic degradation of methyl red and thymol blue using titania–alumina–zinc ferrite nanocomposite, Appl. Catal. B 107 (2011) 333–339.
[18] Z. He, Y. Xia, B. Tang, J. Su, Fabrication and photocatalytic property of magnetic $NiFe_2O_4$/Cu_2O Composites, Mater. Res. Express 4 (2017), 095501.
[19] F. He, A.Y. Meng, B. Cheng, W. Ho, J.G. Yu, Enhanced photocatalytic H2-production activity of WO3/TiO2 stepscheme heterojunction by graphene modification, Chin J Catal 41 (2020) 9–20.
[20] Z. Hea, Y. Xia, B. Tang, J. Su, Fabrication and photocatalytic property of magnetic NiFe2O4/Cu2O composites, Mater. Res. Express 4 (2017), 095501.
[21] D.Q. Hung, N.K. Thanh, Preparation of NiFe2O4 – TiO2 nanoparticles and study of their photocatalytic activity, VNU J. Sci., Matherm. – Phys. 27 (2011) 204–211.
[22] Ö. Kerkez-Kuyumcu, E. Kibar, K. Dayıoğlu, F. Gedik, A.N. Akın, Ş. Özkara-Aydınoğlu, A comparative study for removal of different dyes over M/TiO2 (M = Cu, Ni Co, Fe, Mn and Cr) photocatalysts under visible light irradiation, J. Photochem. Photobiol., A 311 (2015) 176–185.
[23] A. Kezzim, N. Nasrallah, A. Abdi, M. Trari, Visible light induced hydrogen on the novel hetero-system $CuFe_2O_4$/TiO_2, Energ. Convers. Manag. 52 (2011) 2800–2806.
[24] H.S. Kim, D. Kim, B.S. Kwak, G.B. Han, M.H. Um, M. Kang, Synthesis of magnetically separable core@shell structured $NiFe_2O_4$@TiO_2 nanomaterial and its use for photocatalytic hydrogen production by methanol/water splitting, Chem. Eng. J. 243 (2014) 272–279.
[25] N. Kislov, S.S. Srinivasan, Y. Emirov, E.K. Stefanakos, Optical absorption red and blue shifts in $ZnFe_2O_4$ nanoparticles, Mater. Sci. Eng. B 153 (2008) 70–77.
[26] Komaraiah, D. Radha *E.*, Sivakumar J., Reddy M.V. R., Sayanna R. (2020) Photoluminescence and photocatalytic activity of spin coated Ag+ doped anatase TiO2 thin films, *Opt. Mater.*, 108, 110401 (1–14).
[27] P. Laokul, V. Amornkitbamrung, S. Seraphin, S. Maensiri, Characterization and magnetic properties of nanocrystalline CuFe 2O4, NiFe2O4, ZnFe2O4 powders prepared by the Aloe vera extract solution, Curr. Appl Phys. 11 (1) (2011) 101–108.
[28] Z. Li, D. Jin, Z. Wang, Construction of CeO2/CdSe-Diethylenetriamine step-scheme heterojunction for photocatalytic hydrogen production, Int. J. Hydrogen Energy 46 (9) (2021) 6358–6368.
[29] B. Liu, X. Wang, G. Cai, L. Wen, Y. Song, X. Zhao, Low temperature fabrication of V-doped TiO_2 nanoparticles, structure and photocatalytic studies, J. Hazard. Mater. 169 (1–3) (2009) 1112–1118.
[30] R. Liu, H. Yoshida, S. Fujita, M. Arai, Photocatalytic hydrogen production from glycerol and water with NiO_x/TiO_2 catalysts, Appl. Catal. B 144 (2014) 41–45.
[31] Y. Lu, H.-C. Wang, X. She, D. Huang, Y. Yang, X. Gao, Z. Zhu, X. Liu, Z. Xie, A novel preparation of GO/$NiFe_2O_4$/TiO_2 nanorod arrays with enhanced photocatalytic activity for removing unsymmetrical dimethylhydrazine from water, Mater. Sci. Semicond. Process. 121 (2021), 105448.
[32] G. Nabiyouni, M.J. Fesharaki, A. Zolotovsky, Preparation, magnetic studies and band structure calculation of $NiFe_2O_4$ nanoparticles, Task Quarterly 15 (1) (2010) 107–120.
[33] A. Nawaz, A. Rani, H. Zarrin, P. Saravanan, Construction of highly efficient separable p-n junction based light driven composite (NiFe2O4/MnWO4) for improved solar light utilisation, Colloids Surf., A 642 (2022), 128716.
[34] S. Oros-Ruiz, R. Zanella, R. Lopez, A. Hernandez-Gordillo, R. Gomez, Photocatalytic hydrogen production by water/methanoldecomposition using Au/TiO_2 prepared by deposition–precipitation with urea, J. Hazard. Mater. 263 (2013) 2–10.
[35] S. Rana, R.S. Srivastava, M.M. Sorensson, R.D.K. Misra, Synthesis and characterization of nanoparticles with magnetic core and photocatalytic shell: Anatase TiO2–NiFe2O4 system, Mater. Sci. Eng., B 119 (2) (2005) 144–151.
[36] P.A.K. Reddy, S. Basavaraju, D.K. Valluri, V.S. Muthukonda, S. Machiraju, J.S. Lee, $CaFe_2O_4$ sensitized hierarchical TiO_2 photo composite for hydrogen production under solar light irradiation, Chem. Eng. J. 247 (2014) 152–160.
[37] G. Rekhila, Y. Bessekhouad, M. Trari, Visible light hydrogen production on the novel ferrite $NiFe_2O_4$, Int. J. Hydrog. Energy. 38 (2013) 6335–6343.
[38] A.K.L. Sajjad, S. Shamaila, B. Tian, F. Chen, J. Zhang, Comparative studies of operational parameters of degradation of azo dyes in visible light by highly efficient WO_x-TiO_2 photocatalyst, J. Hazard. Mater. 177 (2010) 781–791.
[39] P. Sathishkumar, R.V. Mangalaraja, S. Anandan, M. Ashokkumar, $CoFe_2O_4$/TiO_2 nanocatalysts for the photocatalytic degradation of Reactive Red 120 in aqueous solutions in the presence and absence of electron acceptors, Chem. Eng. J. 220 (2013) 302–310.
[40] W. Septina, S. Ikeda, M.A. Khan, T. Hirai, T. Harada, M. Matsumura, L.M. Peter, Potentiostatic electrodeposition of cuprous oxide thin films for photovoltaic applications, Electrochim. Acta 56 (2011) 4882–4888.
[41] J. Shi, X. Yan, H.-J. Cui, X. Zong, M.-L. Fu, S. Chen, L. Wang, Low-temperature synthesis of CdS/TiO_2 composite photocatalysts: Influence of synthetic procedure on photocatalytic activity under visible light, J. Mol. Catal. A: Chem. 356 (2012) 53–60.
[42] N. Singh, R.M. Mehra, A. Kapoor, Synthesis and characterization of ZnO nanoparticles, J. Nano-Electron. Phys. 3 (2011) 132–139.
[43] T. Somanathan, A. Abilarasu, J.B. Rabindran, V. Ravinayagam, D. Suresh, Microwave assisted green synthesis $Ce_{0.2}Ni_{0.8}Fe_2O_4$ nanoflakes using calotropis gigantean plant extract and its photocatalytic activity, Ceram. Int. 45 (2019) 18091–18098.
[44] T. Sugimoto, X. Zhou, A. Muramatsu, Synthesis of uniform anatase TiO_2 nanoparticles by gel–sol method 3. Formation process and size control, J. Colloid Interface Sci. 259 (2003) 43–52.
[45] A. Šutka, T. Käämbre, R. Pärna, N. Döbelin, M. Vanags, M. Smits, V. Kisand, Ag sensitized TiO2 and NiFe2O4 three-component nanoheterostructures: Synthesis, electronic structure and strongly enhanced visible light photocatalytic activity, RSC Adv. 6 (23) (2016) 18834–18842.
[46] Y. Xia, Z. He, J. Su, B. Tang, K. Hu, Y. Lu, S. Sun, X. Lia, Fabrication of magnetically separable $NiFe_2O_4$/BiOI nanocomposites with enhanced photocatalytic performance under visible-light irradiation, RSC Adv. 8 (2018) 4284–4294.
[47] S. Xu, W. Shangguan, J. Yuan, M. Chen, J. Shi, Preparations and photocatalytic properties of magnetically separable nitrogen-doped TiO_2 supported on nickel ferrite, Appl. Catal. B 71 (3–4) (2007) 177–184.

[48] J. Xu, Y. Ao, D. Fu, A novel Ce, C-codoped TiO_2 nanoparticles and its photocatalytic activity under visible light, Appl. Surf. Sci. 256 (2009) 884–888.
[49] F. Yakuphanoğlu, Electrical characterization and device characterization of ZnO microring shaped films by sol–gel method, J. Alloys Compd. 507 (2010) 184–189.
[50] J. Yan, L. Zhang, H. Yang, Y. Tang, Z. Lu, S. Guo, Y. Dai, Y. Han, M. Yao, $CuCr_2O_4$/TiO_2 heterojunction for photocatalytic H_2 evolution under simulated sunlight irradiation, Sol. Energy 83 (2009) 1534–1539.
[51] X. Yang, C. Cao, L. Erickson, K. Hohn, R. Maghirang, K. Klabunde, Photo-catalytic degradation of Rhodamine B on C-, S-, N-, and Fe-doped TiO_2 under visible-light irradiation, Appl. Catal. B: Environmental 91 (2009) 657–662.
[52] C. Wang, C. Böttcher, D.W. Bahnemannc, J.K. Dohrmann, A comparative study of nanometer sized Fe(III)-doped TiO2 photocatalysts: synthesis, characterization and activity, J. Mater. Chem. 13 (2003) 2322–2329.
[53] Y. Wang, C. Feng, Z. Jin, J. Zhang, J. Yang, S. Zhang, A novel N-doped TiO_2 with high visible light photocatalytic activity, J. Mol. Catal. A: Chem. 260 (2006) 1–3.
[54] S. Wang, S. Zhou, Photodegradation of methyl orange by photocatalyst of CNTs/P-TiO_2 under UV and visible-light irradiation, J. Hazard. Mater. 185 (2011) 77–85.
[55] Y. Wang, X. Meng, Q. Hu, M. Zhang, X. Cao, C. Xu, Y. Ding, Visible-light driven $ZnIn_2S_4$/TiO_{2-x} heterostructure for boosting photocatalytic H_2 evolution, Int. J. Hydrogen Energy 46 (2021) 6262–6271.
[56] L. Zhang, Y. He, Y. Wu, T. Wu, Photocatalytic degradation of RhB over $MgFe_2O_4$/TiO_2 composite materials, Mater. Sci. Eng., B 176 (2011) 1497–1504.
[57] L. Zhang, J. Zhang, H. Yu, J. Yu, Emerging S-scheme photocatalyst, Adv. Mater. 34 (2022) 2107668.
[58] X. Zhu, F. Zhang, M. Wang, J. Ding, S. Sun, J. Bao, C. Gao, Facile synthesis, structure and visible light photocatalytic activityof recyclable $ZnFe_2O_4$/TiO_2, Appl. Surf. Sci. 319 (2014) 83–89.